In-situ Observation of Riming in Mixed-Phase Clouds using the PHIPS probe

Fritz Waitz[a] Martin Schnaiter[a,b] Thomas Leisner[a] Emma Järvinen[a]

[a] *Institute of Meteorology and Climate Research, Karlsruhe Institute of Technology, Karlsruhe, Germany* [b] *schnaiTEC GmbH, Bruchsal, Germany*

Corresponding author: Fritz Waitz, fritz.waitz@kit.edu

ABSTRACT: Mixed-phase clouds consist of both supercooled liquid water droplets and solid ice crystals. Despite having a significant impact on Earth‘s climate, mixed-phase clouds are poorly understood and not well represented in climate prediction models. One piece of the puzzle is understanding and parameterizing riming of mixed-phase cloud ice crystals, which is one of the main growth mechanisms of ice crystals via the accretion of small, supercooled droplets. Especially the extent of riming on ice crystals smaller than 500 µm is often overlooked in studies - mainly because observations are scarce. Here, we investigated riming in mixed-phase clouds during three airborne campaigns in the Arctic, the Southern Ocean and US east coast. Riming was observed from stereo-microscopic cloud particle images recorded with the Particle Habit Imaging and Polar Scattering (PHIPS) probe. We show that riming is most prevalent at temperatures around -7°C, where, on average, 43% of the investigated particles in a size range from $100 \leq D \leq 700$ µm showed evidence of riming. We discuss the occurrence and properties of rimed ice particles and show the correlation of the occurrence and the amount of riming with ambient microphysical parameters. We show that riming fraction increases with ice particle size (<20% for $D \leq 200$ µm, 35-40% for $D \geq 400$ µm) and liquid water content (25% for LWC ≤ 0.05 g m^{-3}, up to 60% for LWC = 0.5 g m^{-3}). We investigate the ageing of rimed particles and the difference between "normal" and "epitaxial" riming based on a case study.

1. Introduction

Mixed-phase clouds (MPCs), consisting of both supercooled liquid droplets and ice particles, play a major role in the atmospheric hydrological cycle and the radiative balance of the Earth (e.g. Korolev et al. 2017). Despite their widespread occurrence, mixed-phase cloud processes are still rather poorly understood and represent a great source of uncertainty for climate predictions (e.g. McCoy et al. 2016).

One important microphysical process in MPCs is *riming*, i.e. the accretion of small supercooled liquid droplets on the surface of ice particles (see example in Fig. 1a). Besides vapor deposition and aggregation, it is one of the three main ice growth modes. Riming can be divided into two (not always easily distinguishable) sub-topics: riming of small ice particles (diameter $D \simeq 100$ - 1000 µm) in clouds and riming of large ($1000 \lesssim D \lesssim 5000$ µm) precipitating ice, graupel, snow particles or frozen precipitation size droplets that collect smaller cloud droplets or slower falling ice particles (e.g. "*ice lollies*" (Keppas et al. 2017)). Whereas most recent publications focus on the latter aspect (riming of large precipitating particles), in this study, we focus on riming of smaller ice particles in clouds.

The typical life-cycle of an exemplary rimed particle is usually as follows: The ice particle is formed, followed by growth via vapor deposition until the particle has reached a critical minimum size for riming (depending on shape and habit, e.g. $D \geq 60$ µm for columns, (e.g. Ono 1969; Ávila et al. 2009)). If liquid droplets are present in large enough numbers, the ice particle starts collecting supercooled droplets (around $D = 10 - 40$ µm, e.g. Harimaya (1975)) that freeze on the particle's surface. When the ice particle has acquired enough mass so gravitational settling becomes efficient, it precipitates and accretes even more droplets whilst falling and grows further until it reaches the ground as graupel.

Ice particle growth, both in size and mass, can ultimately change cloud lifetime and radiative properties. The scavenging of supercooled liquid water affects droplet size distribution and number concentration and thus liquid water content as well as aerosol concentration (Baltensperger et al. 1998; Hegg et al. 2011). Also, splintering during the riming process can initiate secondary ice formation, thus leading to the formation of new ice particles known as the *Hallett-Mossop-process* (e.g. Hallett and Mossop 1974; Korolev et al. 2020; Field et al. 2017). Since rimed ice particles are of higher mass and more compact compared to unrimed particles, their fall speed and terminal velocity are increased relative to equivalent unrimed particles (Locatelli and Hobbs 1974; Lin et al. 2011; Garrett and Yuter 2014). Furthermore, riming leads to increased surface roughness and complexity, and hence affects the ice particles' radiative properties, as shown in e.g. Schnaiter et al. (2016); Järvinen et al. (2018); Järvinen et al. (2021).

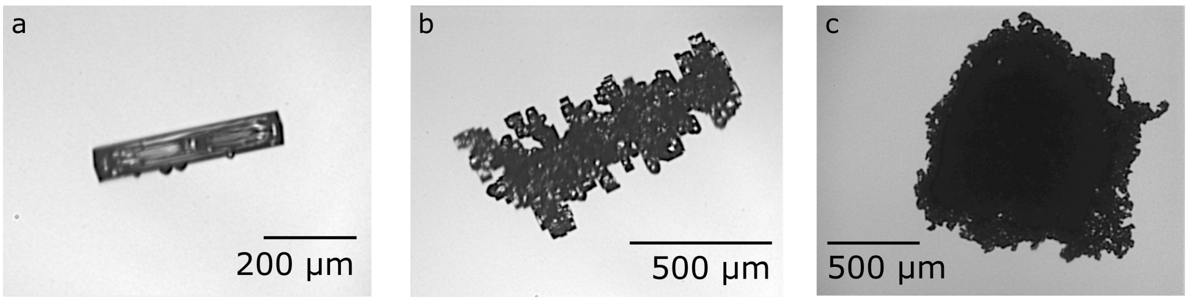

Fig. 1. Example of a (a) slight "normally" rimed , (b) heavily "epitaxially" rimed column and (c) a graupel particle captured by the PHIPS probe during the IMPACTS campaign.

In principle, riming can occur everywhere where ice particles and supercooled droplets coexist. Pflaum and Pruppacher (1979) have defined the collection kernel of a collector with radius R and a droplet with radius r that have a relative velocity Δv against each other as

$$K = E_1 E_2 \pi (r+R)^2 \Delta v \tag{1}$$

where E_1 is the collision efficiency of the two particles and E_2 the efficiency that the two particles remain attached to each other. Ice-ice collisions can lead to aggregation, droplet-droplet collisions to coalescence and ice-droplet collisions to riming. For riming, these quantities depend on numerous parameters including temperature (Kneifel and Moisseev 2020), humidity (Khain et al. 1999), habit, size and orientation of the ice particle (Ono 1969; Wang and Ji 2000; Ávila et al. 2009), number and size distribution of the supercooled droplets (Saleeby and Cotton 2008) as well as turbulence and vertical velocity (Herzegh and Hobbs 1980; Garrett and Yuter 2014). The amount of rime on an ice particle is hence dependent on all these quantities throughout particle's trajectory in the cloud and during precipitation.

In recent years, multiple studies have used radar measurements to retrieve information about snow and riming density based on their vertical Doppler velocity (Mosimann et al. 1993; Leinonen and Szyrmer 2015; Leinonen et al. 2018; Mason et al. 2018; Kneifel and Moisseev 2020). Those methods proved to be fit to determine the riming state (i.e. whether a particle is rimed or unrimed) of large, precipitating snow and graupel particles. However, they cannot resolve the fine structure of small or freshly rimed ice particles inside clouds if the radar signal is dominated by large graupel particles in the size range $D = 1 - 10\,\mathrm{mm}$. In-situ studies with high-resolution cloud imaging probes investigating the properties of individual rimed particles sampled directly in the cloud, however, are scarce. The difficulty is to resolve riming features and discriminate between rimed and non-rimed irregular particles. Furthermore, analysis of particle images is quite complex and hence automated and manual assessment of particle properties is very laborious. Consequently, the riming of ice particles is often poorly or not at all represented in climate prediction models. So far, the exact processes influencing the riming of could particles are not well understood. A deterministic parameterization of when and where to expect how much riming does not exist. Most models account for the riming degree (i.e. what fraction of a crystal's surface is covered by rime) only in the sense of a *subtype* for hydrometeors (e.g. *cloud ice, graupel, snow* in COSMO, Blahak and Seifert (2015), http://www.cosmo-model.org/). Furthermore, riming is neglected completely in most Arctic model studies (e.g. Fan et al. 2011; Ovchinnikov et al. 2014; Stevens et al. 2018).

In this work, we investigate riming of ice particles using the Particle Habit Imaging and Polar Scattering (PHIPS) probe. PHIPS is an aircraft-mounted cloud probe acquiring stereo-microscopic images and corresponding angular scattering functions of single cloud particles in the size range $D = 20 - 700\,\mu\mathrm{m}$ and $D = 50 - 700\,\mu\mathrm{m}$ for ice and droplets, respectively. With its high optical resolution and single particle measurements, PHIPS is well suited to investigate detailed features like riming of individual ice particles. We present microphysical observations of ice particles from three field campaigns investigating high latitude MPC. In section 2, we give an overview of the three field campaigns as well as a brief introduction of the PHIPS probe and its data analysis methods. Combining the data from these three field campaigns, an extensive data-set observing ice particles of various size, habit and riming state has been acquired. In section 3, we present a statistical analysis of the correlation with ambient conditions of rimed particles for different degrees of riming. We estimate the minimum size of rimed particles as well as droplets, confirming the results of previous laboratory studies. Further, we highlight various riming features such as one-sided rimed plates or "*ice lollies*". One particularly interesting observation is ice particles carrying small, faceted rime oriented to the crystalline axis of the host particle. Such particles have been observed before (Korolev et al. 2020) but their occurrence and properties have not been studied comprehensively. This type of riming, which we call *Epitaxial Riming* and which is e.g. shown in Fig. 1b, will be analyzed in detail in section 4 including a case study showing the typical step-by-step evolution of epitaxially rimed particles.

2. Methods and Experimental Data Set

a. Campaigns

In this work, we use experimental in-situ data gathered during three airborne field campaigns:

1. ACLOUD - Arctic CLoud Observations Using airborne measurements during polar Day, May/June 2017 based in Svalbard (Spitsbergen, Norway) with the AWI Polar6 aircraft (165 flight hours),

2. SOCRATES - Southern Ocean Clouds, Radiation, Aerosol Transport Experimental Study, Jan/Feb 2018 based in Hobart (Tasmania, Australia) with the NCAR Gulfstream-V aircraft (105 flight hours) and

3. IMPACTS - Investigation of Microphysics and Precipitation for Atlantic Coast-Threatening Snowstorms, Jan/Feb 2020 based in Wallops (VA, USA) with the NASA P3 aircraft (53 flight hours).

An overview of the microphysical conditions as well as the instrumentation during those campaigns can be found in Knudsen et al. (2018) and Wendisch et al. (2019) for ACLOUD, McFarquhar et al. (2019) for SOCRATES and McMurdie et al. (2019) for IMPACTS. The sampling during those three campaigns includes a wide variety of different cloud conditions: warm clouds, supercooled liquid clouds, ice clouds and mixed-phase clouds. Clouds sampled ranged in altitude from boundary layer clouds below 200 m to mid-level clouds between 4000 m and 6000 m asl. Temperatures ranged from -20 to +5°C during ACLOUD, -35 to +5°C during SOCRATES and -32 to +9°C during IMPACTS. The sampled ice particles covered a wide range of different particle shapes and habits (columns, plates, needles, bullet rosettes, dendrites and irregulars, including rough, rimed and pristine particles) as well as sizes from $D = 20 - 700\,\mu\text{m}$. The instrumentation on the three aircraft included cloud particles probes such as the SID-3 (*Small Ice Detector Mk. 3*), CDP (*Cloud Droplet Probe*, DMT, Longmont, USA), CIP (*Cloud Imaging Probe*, DMT, Longmont, USA) and PIP (*Precipitation Imaging Probe*, DMT, Longmont, USA) during ACLOUD, 2DS, 2DC (*Two-dimensional Stereo Probe*, *Two-dimensional Cloud Probe*, SPEC Inc., Boulder, USA) and CDP during SOCRATES and 2DS, CDP and CPI (*Cloud Particle Imager*, SPECinc, Boulder, CO, USA) during IMPACTS.

For SOCRATES, vertical Doppler velocity was measured by the HCR (HIAPER cloud Radar, UCAR/NCAR-EOL (2022)) which has a transmit frequency 94.40 GHz (W-band), temporal resolution 10 Hz, vertical range resolution of 20 to 180 m and a typical radial velocity uncertainty of 0.2 $\mathrm{m\,s^{-1}}$ at a Doppler velocity of $w = 2\,\mathrm{m\,s^{-1}}$). The velocity data is corrected for aircraft motion and aliasing-bias. The ambient temperature was measured with a heated temperature sensor (Harco 149 Model 100009-1 Deiced TAT) that has a general accuracy of 0.3°C. The vertical velocity was measured using a Radome air-motion system (UCAR/NCAR-Earth Observing Laboratory 2019). Relative humidity was measured by the VCSEL (Vertical-Cavity Surface-Emitting Laser hygrometer) with an uncertainty ranging from 6% to 10% (Diao 2021). During ACLOUD, the temperature was measured using an open-wire Pt100 in an unheated Rosemount housing at the tip of the noseboom with a frequency of 100 Hz and an estimated accuracy of ±0.1°C. The vertical wind was measured using a Rosemount 858 five-hole probe with a relative accuracy of the vertical wind speed of ±0.05 m/s for straight and level flight sections. During IMPACTS, atmospheric state measurements were performed using the Rosemount Total Air Temperature (TAT) probe and the Edgetech three-stage chilled mirror hygrometer with 1Hz temporal resolution (Martin and Bennett 2020). For each particle observed by PHIPS, the corresponding temperature, humidity and velocity data as well as LWC were determined as the average over $t = t_s \pm 0.5$ s around the time of acquisition t_s where each PHIPS particle was sampled.

Due to the variability of the microphysical conditions and sampled particles, the data gathered during these three campaigns provide a suitable and representative data set for a comprehensive characterization of riming in mixed-phase clouds. All data cited in this work can be found in the corresponding data bases for the three campaigns: Ehrlich et al. (2019) for ACLOUD, EOL (2018) for SOCRATES, McMurdie et al. (2019) for IMPACTS.

b. The PHIPS Probe

PHIPS is designed to investigate the microphysical and light scattering properties of cloud particles. It produces microscopic stereo-images whilst simultaneously measuring the corresponding angular scattering function for the angular range from 18° to 170° for single cloud particles. More information and a detailed characterization of the PHIPS setup and instrument properties can be found in depth in Abdelmonem et al. (2016) and Schnaiter et al. (2018). From the stereo images, single-particle microphysical features such as e.g. area equivalent diameter or aspect ratio, can be obtained. The image analysis algorithm is explained in depth in Schön et al. (2011). Based on the single-particle's angular scattering function, the thermodynamic phase and the scattering equivalent diameter can be derived as explained in Waitz et al. (2021).

For ACLOUD and SOCRATES, the instrument settings were set to measure single cloud particles in a size range from $50\,\mu m \leq D \leq 700\,\mu m$ and $20\,\mu m \leq D \leq 700\,\mu m$ for droplets and ice particles, respectively. The image acquisition rate of the microscopic system was limited to 3 Hz in these campaigns, while singe-particle scattering data could be acquired up to a maximum rate of 3.5 kHz. The magnification settings of the cameras corresponded to an optical resolution of approximately 3.3 µm. Since PHIPS characterizes individual particles, it has a narrow sensitive area (A_{sens}). As discussed in Waitz et al. (2021), A_{sens} is size dependent (e.g., $A_{sens} = 0.5\,mm^2$ for ice particles with $D = 200\,\mu m$). Assuming a relative flight speed of $v_s = 150\,m\,s^{-1}$, this corresponds to a sampling volume of $V_{sens} = A_{sens} \cdot v_s = 0.08\,L\,s^{-1}$. During IMPACTS, the scientific focus was on larger ice crystals so the trigger threshold as well as the magnification were increased to trigger only particles larger than $D \geq 100\,\mu m$ for droplets and $D \geq 40\,\mu m$ for ice. The magnification settings of the cameras corresponded to an optical resolution of approximately 4 µm and the maximum camera acquisition rate was varied between 3 to 10 Hz, which corresponds to a maximum spatial resolution of roughly one stereo-image per 15 m.

c. Manual Image Classification

All PHIPS stereo-images from the ACLOUD and SOCRATES data-sets were visually classified into seven habit classes: (i) plate-like particles (single plates, sectored plates, skeleton plates and side planes), (ii) columnar particles (solid columns, hollow columns and sheaths), (iii) needles, (iv) frozen droplets, (v) bullet rosettes, (vi) graupel, and (vii) irregular particles. In addition to the habits, the particles were assigned the attributes *rimed* or *unrimed*. The temperature dependent frequency of occurrence distributions of the different particle habits are shown in the SI (Fig. S1). An overview of the riming fraction and riming type (normal, epitaxial, see Sec. 4) per habit is shown in Fig. S2.

In a next classification step, a subset of the well classified particles was again visually classified further regarding their riming features. The second classification step was performed only for particles larger than 100 µm sampled at a temperature $T \geq -17°C$. Smaller particles were almost exclusively small irregulars whose riming state could not be classified with certainty due to the limited optical resolution and almost no riming was observed at lower temperatures, see Fig.4a. CDP LWC ranged from 0 g/m3 to 0.5 g/m3 and vertical HCR Doppler velocity from -4 m/s to +2 m/s (negative velocity corresponds to downward direction, positive to upward direction).

Particles were classified regarding their surface riming degree (SRD) as (i) unrimed (SRD = 0%, no visible riming on any of the two stereo-micrographs), (ii) slightly rimed (SRD < 25%, a few scattered rime particles on the crystal's surface), (iii) moderately rimed (25% ≤ SRD ≤ 50%, up to half of the particle's surface is covered by rime), (iv) heavily rimed (50% < SRD < 100%, most of the particle's surface is covered by rime) as well as (v) graupel (SRD = 100%, the whole particle surface is covered by multiple layers of rime, so that the structure of the underlying particle is no longer recognizable). Exemplary PHIPS particles from these classes are shown in Figs. 2 and 3. This classification approach is similar to the definition of riming degree used in previous studies such as Magono and Lee (e.g. 1966); Bruintjes et al. (e.g. 1987); Mosimann et al. (e.g. 1993, 1994); Mosimann (e.g. 1995). Also, the attributes (i) one-sided riming and (ii) epitaxial riming (which will be explained in detail in section 4) were assigned. As each particle is imaged from two different viewing angles (120° apart), whether or not a particle has rime only on one side can also be assessed for opaque particles (see examples in Fig. 6).

The remaining data-set includes 3,957 particles from ACLOUD and 1,413 from SOCRATES. Examples of particles classified in the different categories are shown in the following section. Manual classification was not applied for the complete IMPACTS data set due to large number of ice particle images (over 250,000 images were acquired). Therefore, only the set of images used for the case study presented in section b was manually inspected.

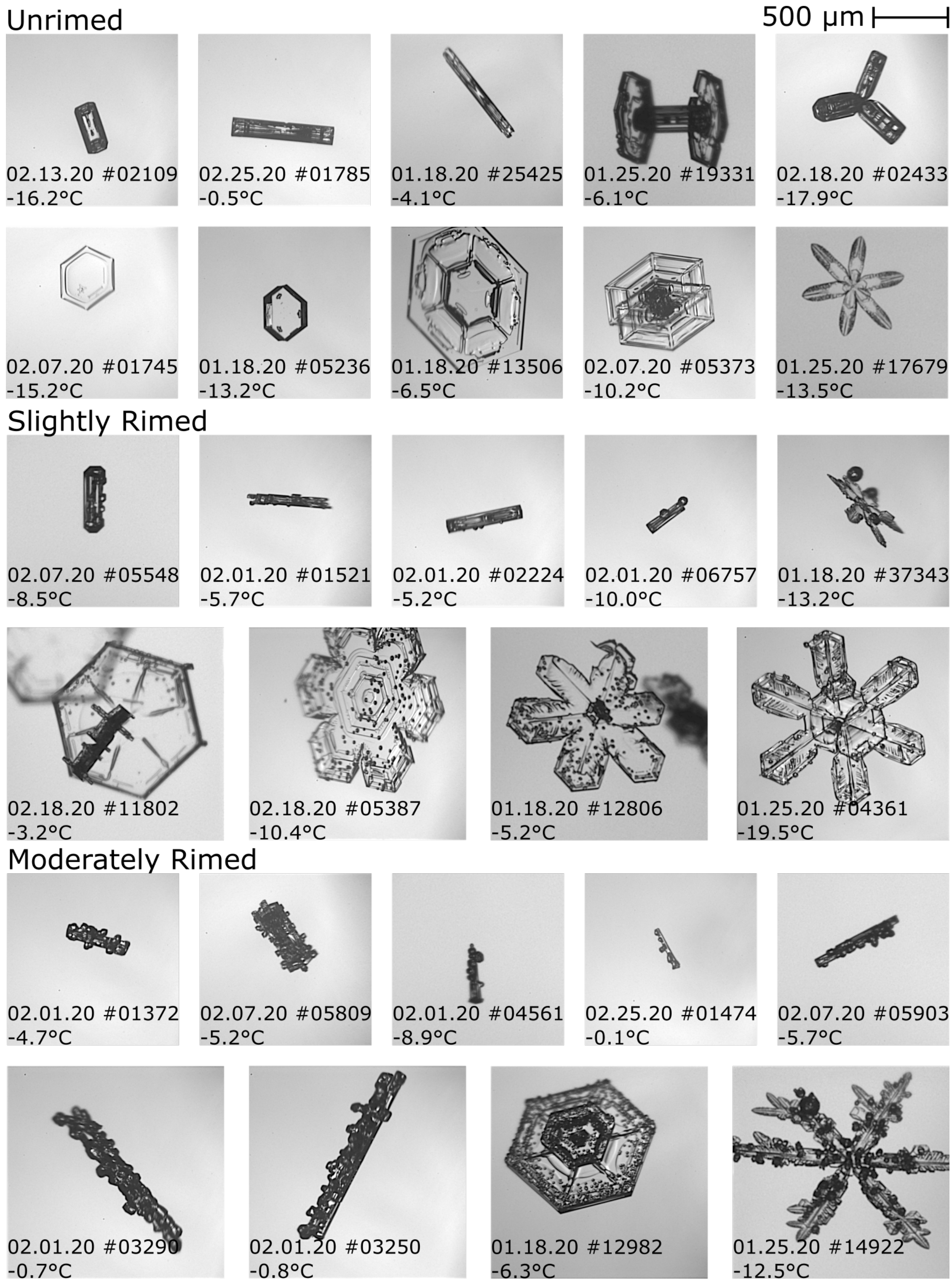

FIG. 2. Examples of representative PHIPS particles with different degrees of riming categorized by the surface riming degree (SRD): unrimed (SRD = 0%), slightly rimed (0% < SRD < 25%) and moderately rimed (25 ≤ SRD ≤ 50%) particles. Heavily rimed (50% < SRD < 100%) and graupel particles (SRD = 100%) are shown in Fig. 3.

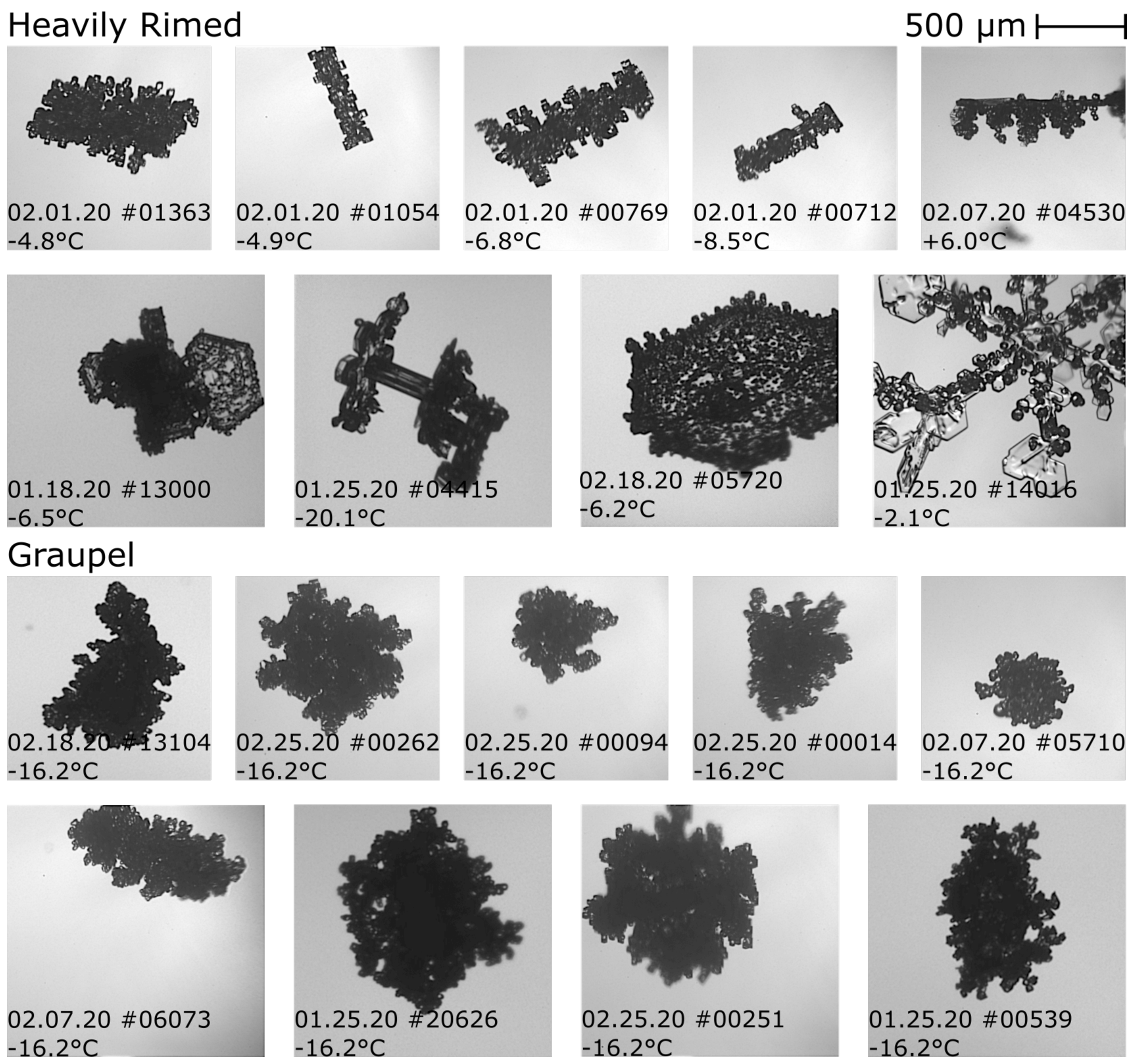

FIG. 3. Examples of representative PHIPS particles with different degrees of riming depending on the surface riming degree (SRD): heavily rimed (50% < SRD < 100%) and graupel particles (SRD = 100%). Unrimed (SRD = 0%), slightly rimed (0% < SRD < 25%) and moderately rimed particles (25 ≤ SRD ≤ 50%) are shown in Fig. 2.

3. Statistical Analysis and Correlation with Ambient Conditions

As discussed in the introduction, riming is dependent on a variety of atmospheric quantities including temperature, humidity and vertical wind velocity as well as trajectory and microphysical properties such as number concentration, size distribution, habit and orientation of ice particles and supercooled droplets. It is not possible to know each of those parameters for each particle at every given moment. Hence, as already mentioned above, such detailed description of riming on a particle-by-particle basis is not present in current climate prediction models and riming is only accounted for in terms of graupel and snow and rarely for smaller, less densely rimed particles. Here, we investigate riming of sub-millimeter ice particles based on in situ aircraft data and correlate the relative occurrence of rimed and unrimed ice particles with other microphysical parameters. Note that the measured conditions do not necessarily represent the environment where the particles experienced riming but rather where they were sampled. This statistical analysis is based on 5,370 manually classified images from the ACLOUD and SOCRATES campaign.

a. Riming Fraction

In the following, "riming fraction" refers to the relative amount of rimed particles compared to total amount of classified ice particles (rimed + unrimed). Fig. 4a shows the correlation of riming fraction and ambient temperature ($R^2 = 0.94$). The corresponding fit parameters for all histograms are shown in Table 1. Most riming was observed in a temperature range between $-10°\mathrm{C} \leq \mathrm{T} \leq 0°\mathrm{C}$ with the maximum around $T \simeq -7°\mathrm{C}$ where up to 55% of all ice particles were rimed. The high riming fraction around −17°C is due to a very high rimed fraction in this temperature bin during a single cloud segment of RF09 of SOCRATES. It is based on a low number of total particles ($n = 213$) and is therefore not assumed to be a generalizable feature.

For the following analysis, apart from Fig. 4a, only particles sampled at $\mathrm{T} \geq -17°\mathrm{C}$ are considered. Fig. 4b shows riming statistics as a function of ice particle's area equivalent diameter retrieved from the stereo-microscopic images. It can be seen that the percentage of rimed particles increases with particle size ($R^2 = 0.96$). The riming fraction increases from below 5% for particles smaller than $D_{\mathrm{im,A}} \leq 150\,\mu\mathrm{m}$ to over 35% for particles larger than $D_{\mathrm{im,A}} \geq 400\,\mu\mathrm{m}$. Above that, the riming fraction is only weakly dependent on particle size. The smallest ice particle where riming was observed was a column with an area equivalent diameter of $\mathrm{D_{im,\,A}} = 116.1\,\mu\mathrm{m}$ and maximum dimension $\mathrm{D_{im,\,max}} = 193.7\,\mu\mathrm{m}$ (shown in Fig. S7 in the SI). This is a larger riming onset size compared to e.g. Ono (1969) and Ávila et al. (2009), who reported a critical minimum diameter of $\mathrm{D} \geq 60\,\mu\mathrm{m}$ for riming on columns collected via glass slides and analyzed by optical microscopy.

The correlation of riming fraction and cloud liquid water content (LWC) measured by the CDP is shown in Fig. 4c ($R^2 = 0.86$). The riming fraction increases from 25% in cloud segments with low LWC below $0.05\,\mathrm{g\,m^{-3}}$ to 60% for $\mathrm{LWC} \geq 0.5\,\mathrm{g\,m^{-3}}$. Rime particles had a size around roughly

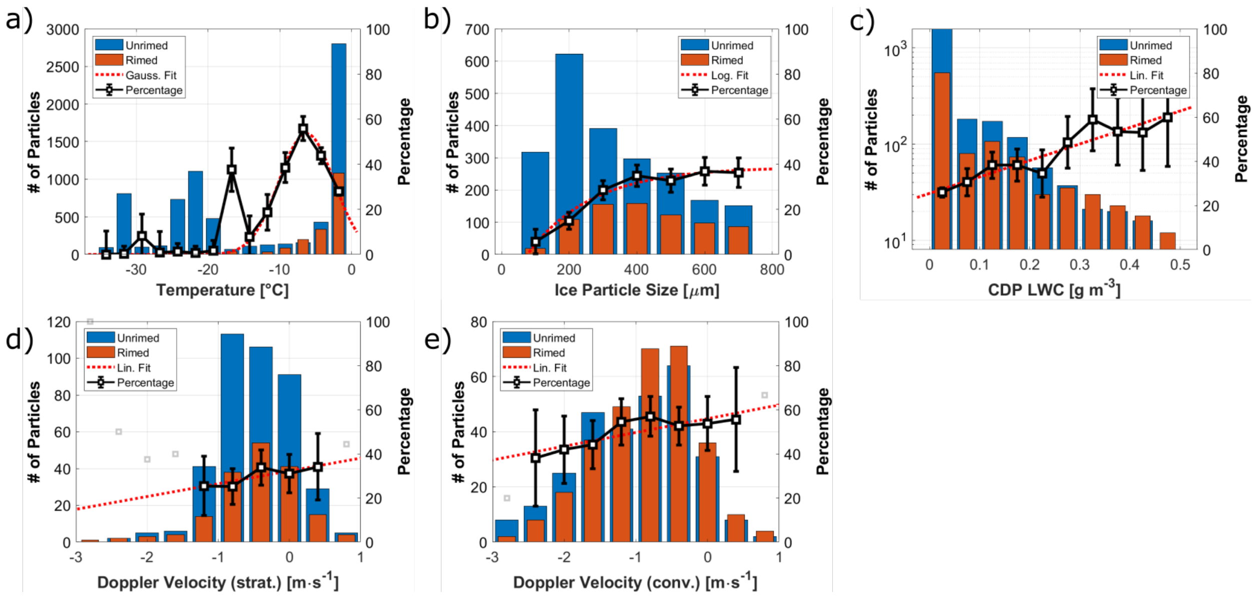

FIG. 4. Histograms showing the absolute number of classified unrimed (blue) and rimed (red) particles during ACLOUD and SOCRATES as well as the riming fraction (relative percentage $n_{\mathrm{rimed}}/n_{\mathrm{all}}$, black, right axis) in correlation with different ambient parameters: Temperature (a), area-eq. diameter of the underlying ice particle measured by PHIPS (b), CDP liquid water content (c) and vertical HCR Doppler velocity in stratiform (d) and convective clouds (e). HCR data is only available for SOCRATES. The red dotted line shows a fit to the riming fraction (right y-axis). The corresponding fit parameters for all histograms are shown in Tab. 1. The statistical uncertainty bars correspond to the number of particles per bin ($n^{-1/2}$). Only bins with $n \geq 20$ are considered for the fit, others are shown in grey. Correlation plots with further parameters (CDP mean droplet diameter, ambient vertical velocity, relative cloud height, relative humidity), which show only a weak dependency, are shown in Fig. S3 in the SI.

TABLE 1. Fit parameters to the riming percentage histograms shown in Fig. 4.

		Fit function	R^2
Temperature		$y = -0.952\ x^2\ -12.2\ x + 11.9$	0.940
Ice particle diameter	(PHIPS)	y = 38.7 - exp[-52.8 (x-769)]	0.964
Liquid water content	(CDP)	y = 74.7 x + 25.5	0.863
Vertical Doppler velocity	(HCR, strat.)	y = 5.79 x + 32.2	0.707
Vertical Doppler velocity	(HCR, conv.)	y = 6.24 x + 55.9	0.724

$D_{\mathrm{max}} \simeq 20$ and 50 μm as shown in Figs. 5a,b for two exemplary ice crystals that were amongst the crystals with the smallest and largest rime particles based on visual inspection. This is in agreement with results presented by Kikuchi and Uyeda (1979) and Harimaya (1975), who reported sizes of rime particles between 10 and 60 µm. As there exists no automated method to determine the size of the rime particles based on the PHIPS images, the size of rime particles is not further investigated in this work. Comparison with CDP mean droplet diameter showed a slight relation with a maximum riming fraction at $D_{drop, mean} = 20$ µm (see Fig. S3f in the SI). Figs. 5c,d show drizzle-rimed ice (*ice lollies*). Such contact freezing of relatively large droplets compared to the size of ice particle was reported by (Uyeda and Kikuchi 1978; Keppas et al. 2017). We also see this in our data set, but there are only very few cases. Due to the low number, no relationship with sampled PHIPS drizzle droplet concentration was found and no detailed statistical analysis was conducted.

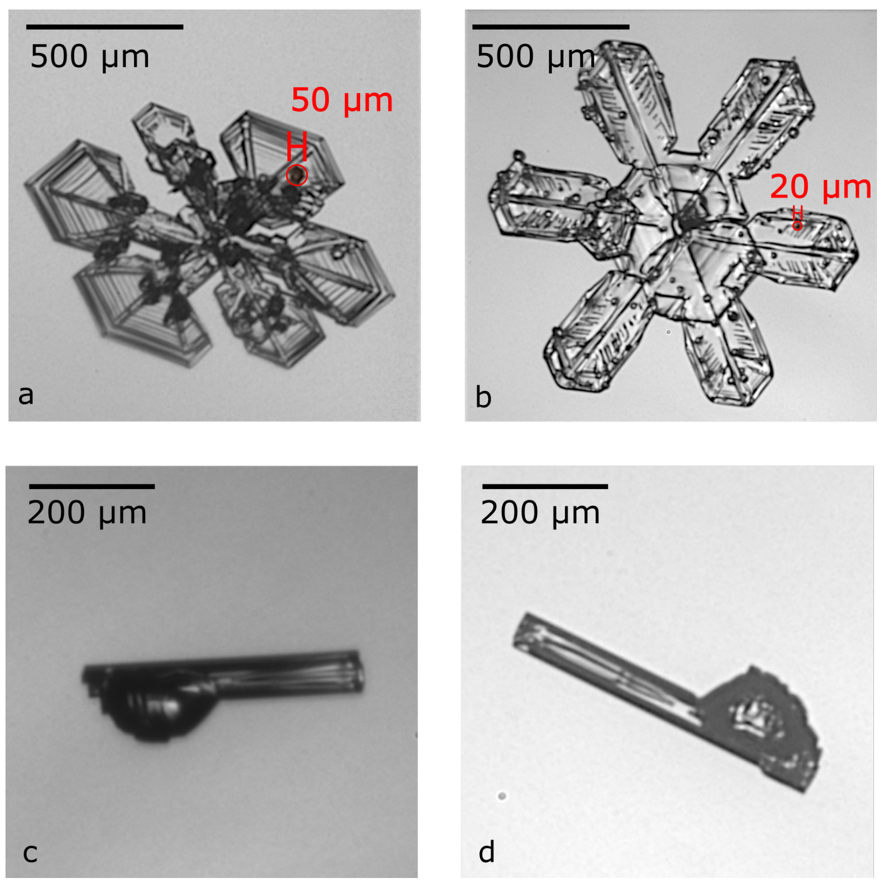

Fig. 5. Exemplary slightly rimed particles showing the size of rime particles on the surface (a, b) and drizzle rimed ice (ice lollies, c,d).

Fig. 4d and e show the correlation ($R^2 = 0.7$) with the Doppler radial velocity measured by the HCR, which is the sum of vertical air velocity and particle fall speed, corrected by the vertical motion of the aircraft. HCR data are only available for the SOCRATES campaign. Since the HCR has a dead zone of 145 m around the aircraft in which data are not usable, there is no data available at the location of the aircraft. Hence, each data point corresponds to the measured HCR Doppler velocity of the first valid gate closest to the aircraft. The HCR was typically rotated to point in zenith direction when flying beneath clouds or ascending through boundary layer clouds and nadir at other times. The sign was adjusted based on HCR orientation so that negative velocity always corresponds to downward direction, positive to upward direction. The analysis was divided into stratiform and convective cloud segments based on the flag given in UCAR/NCAR-EOL (2022). For stratiform cases, events for which the melting layer was close to the position of the aircraft were omitted, since events where in-situ probes and the first gate were not "on the same side" of the melting layer would lead to potentially biased velocities due to the discontinuity at the melting layer (Romatschke 2021; Romatschke and Dixon 2022). It can be seen that there is a clear trend of increasing riming fraction towards more positive (upward) Doppler velocities. Further, on average, the riming fraction is much higher in convective (52%) compared to stratiform clouds (34%). This can be explained by updrafts and in-cloud turbulence, which increases the time and trajectory that the particles remain in the cloud as well as the relative velocity of ice particles against droplets and thus increases the probability that they collide to form riming. Further, both ice particles as well as droplets can grow larger in updrafts due to the increased time they spend in the cloud as well as the typically higher supersaturation values affiliated with updrafts.

The measurement of ambient vertical velocity around the aircraft shows a slight trend towards both higher positive and negative values (see Fig. S3h in the SI). This could indicate a relationship with turbulent air motion, as riming is expected to be more likely if particles remain longer in the cloud, having a longer total travel path and hence a higher chance of collecting droplets. However, at the same time, a lot of one-sided rimed plates were observed during the campaigns (see Fig. 6), which would be unlikely if all riming would necessarily be correlated with turbulent air motion. This confirms observations of fallen snow by Ono (1969) and Rango et al. (2003). Note that the ambient vertical velocity measured at the aircraft is the combination of small-scale turbulence and large-scale vertical motion which cannot be easily disentangled. Roughly 15% of all plates at high temperatures $T > -10°C$ are rimed on one side (see Fig. S6a and the corresponding discussion in the SI) and almost none at lower temperatures. No significant relationship (R^2 below 0.5) or only very minor dependency of riming fraction and CDP droplet number concentration, CDP mean droplet diameter, ambient vertical velocity, relative cloud height and relative humidity were found. The corresponding plots are shown in Fig. S3 in the SI.

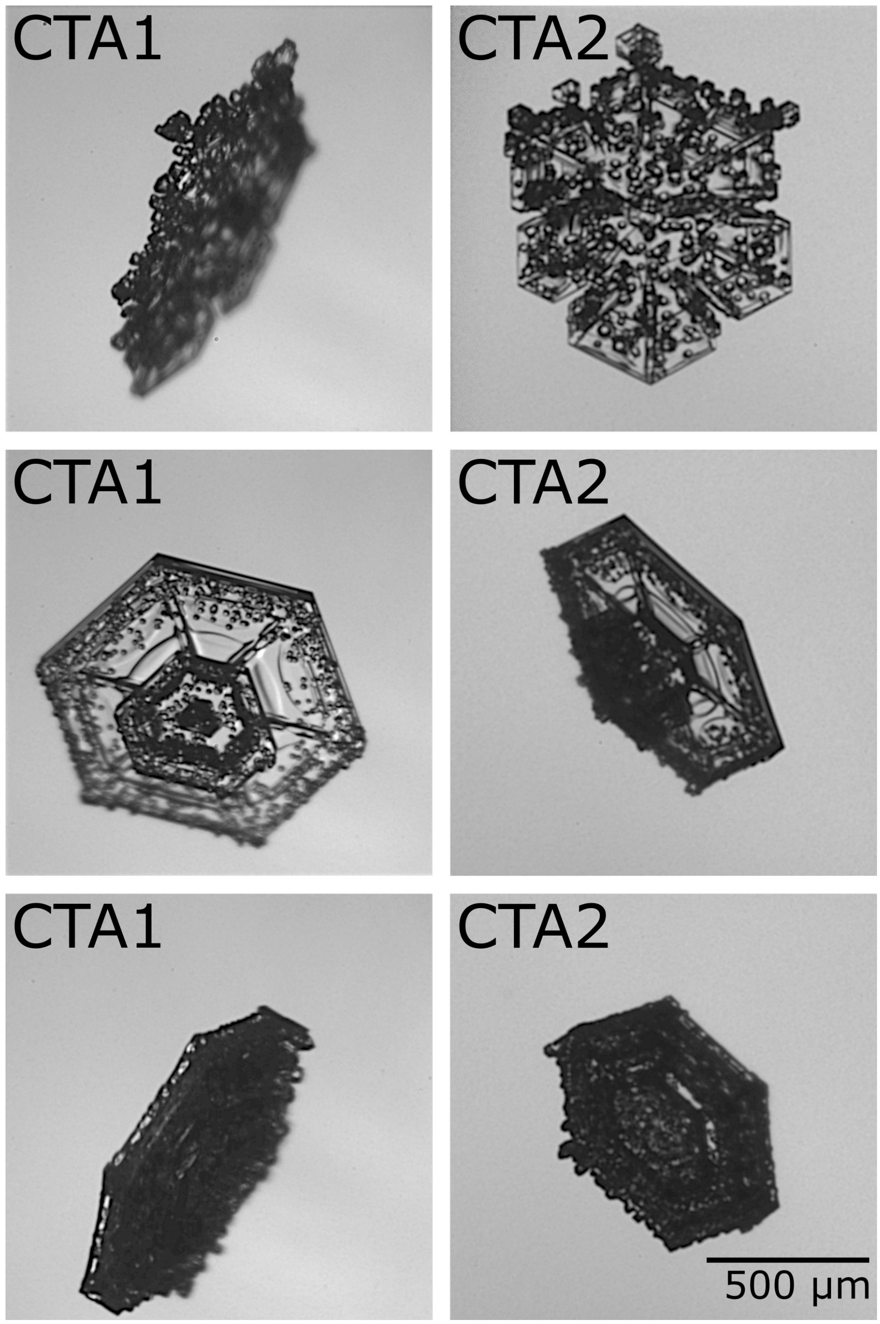

FIG. 6. Three exemplary one-sided, moderately rimed particles shown from different perspectives by the two camera telescope assemblies (CTA1 and CTA2). Note that the particle orientation in the stereo image does not reflect the actual orientation with respect to horizon.

b. Riming Degree

All rimed ice particles were manually classified concerning their *riming degree*, i.e. their estimated surface riming degree. This classification was done manually based on visual inspection of the particle's individual stereo-images. Exemplary particles are shown in Fig. 2.

Fig. 7 shows the relative distribution of SRD with three ambient and microphysical parameters: temperature (Fig. 7a), ice particle area equivalent diameter (Fig. 7b) and vertical Doppler velocity (Fig. 7c,d). A relationship is seen between temperature and SRD. At lower temperatures ice particles are more heavily rimed. At temperatures $T \leq -15°C$, more than 80% of all rimed particles are heavily rimed or graupel, whereas most slightly rimed particles are found at high temperatures between -5 and 0°C.

A positive trend is also visible between SRD and ice particle size: Most small particles around $D_{im,A} \leq 250\,\mu m$ show only slight riming whereas heavy riming is mostly found on larger particles. These typically large heavily rimed and graupel particles relate with an increased negative (downwards) Doppler velocity (Fig. 7c,d) as they are almost spherical and hence more densely packed compared to aspherical ice particles. This is in agreement with Doppler radar studies presented by Mosimann (1995). This effect is weaker for convective clouds (Fig. 7d) compared to stratiform clouds (Fig. 7c). A possible explanation is that the increased fall speed due to the increase SRD cancels out with updrafts of the air parcels that cause the increased SRD in the first place. Comparisons with LWC and the other previously discussed parameters (plots shown in the SI) show no apparent relationship. Since the classification of SRD is only based on visual inspection, no further numerical analysis was conducted and no fit parameters are presented.

4. Epitaxial Riming

Rimed ice particles are usually understood as ice particles that have round accretion (rime). However, during their ageing process, the form of accretion can change significantly. Fig. 8 shows exemplary rimed ice particles with differently structured rime: round rime (Fig. 8a) and crystalline, faceted rime (Fig. 8b-e). The latter can be explained by ageing (vapor deposition growth) of rimed particles. In the following, round rime particles on ice crystal surfaces will be referred to as "*normal riming*".

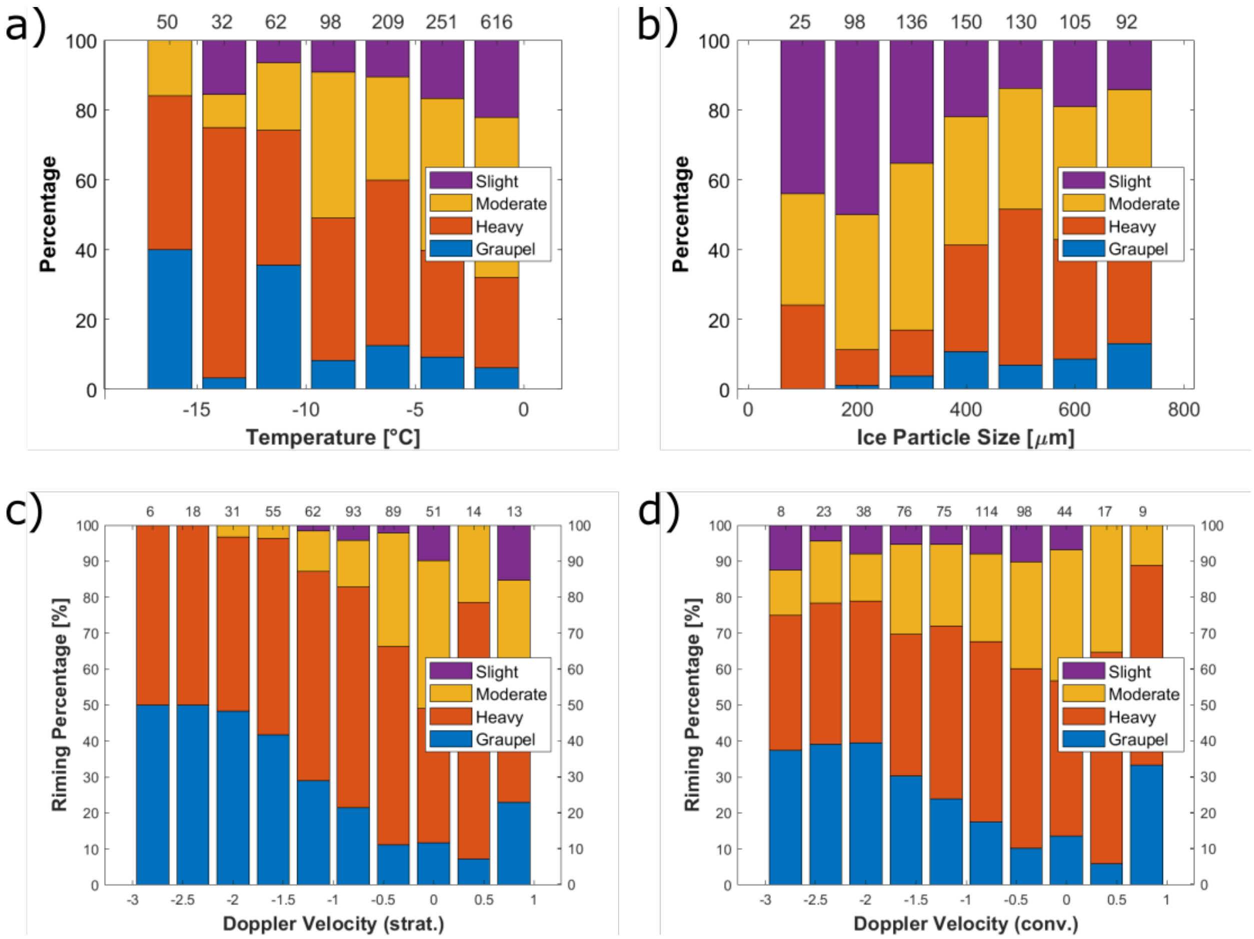

FIG. 7. The relative occurrence of particles of different riming degree as defined in Fig. 2: slight (purple), moderate (yellow) and heavy riming (red) as well as graupel (blue) in relation with ambient temperature (a), ice particle size (b), and HCR Doppler velocity (c,d) similar to Fig. 4. The values on the upper x-axis correspond to the total number of particles per bin.

Particles with faceted rime have been reported in the past. Korolev et al. (2020) have reported a case study with "a few ice particles with small faceted particles stuck to their surfaces", which they refer to as "aged rimed ice particles" that had possibly originated from "vapor deposition regrowth of rime into faceted particles". Libbrecht (2016) has reported "oriented freezing" of rime particles that "freeze with their molecular lattices matching the pre-existing lattice underneath", which results in "faceted rime particles". Since not all aged rimed particles show small faceted particles on the surface and the attribute "faceted" is often used in other context for ice particles (pristine plates, e.g. Libbrecht et al. (2015); Korolev et al. (2020)), we propose the term *"epitaxial* *riming"* to avoid any confusion. In general, epitaxy refers to crystalline growth of a material on the surface of another particle along the lattice structure of the underlying particle (Pashley 1956). The epitaxial growth of ice on the surface of crystalline substrates, such as e.g. feldspar, has been the topic of many previous works (e.g., Bryant et al. 1960; Kiselev et al. 2016). Here, we describe the growth of small ice particles on the surface of larger ice particles along the same crystal axis. Thus, the term "epitaxial riming" refers to faceted, rimed particles, underlining the important property that the small "rimed" particles on the surface inherit the same lattice structure as the underlying host particle and share the same c-axis as shown in Fig. 8.

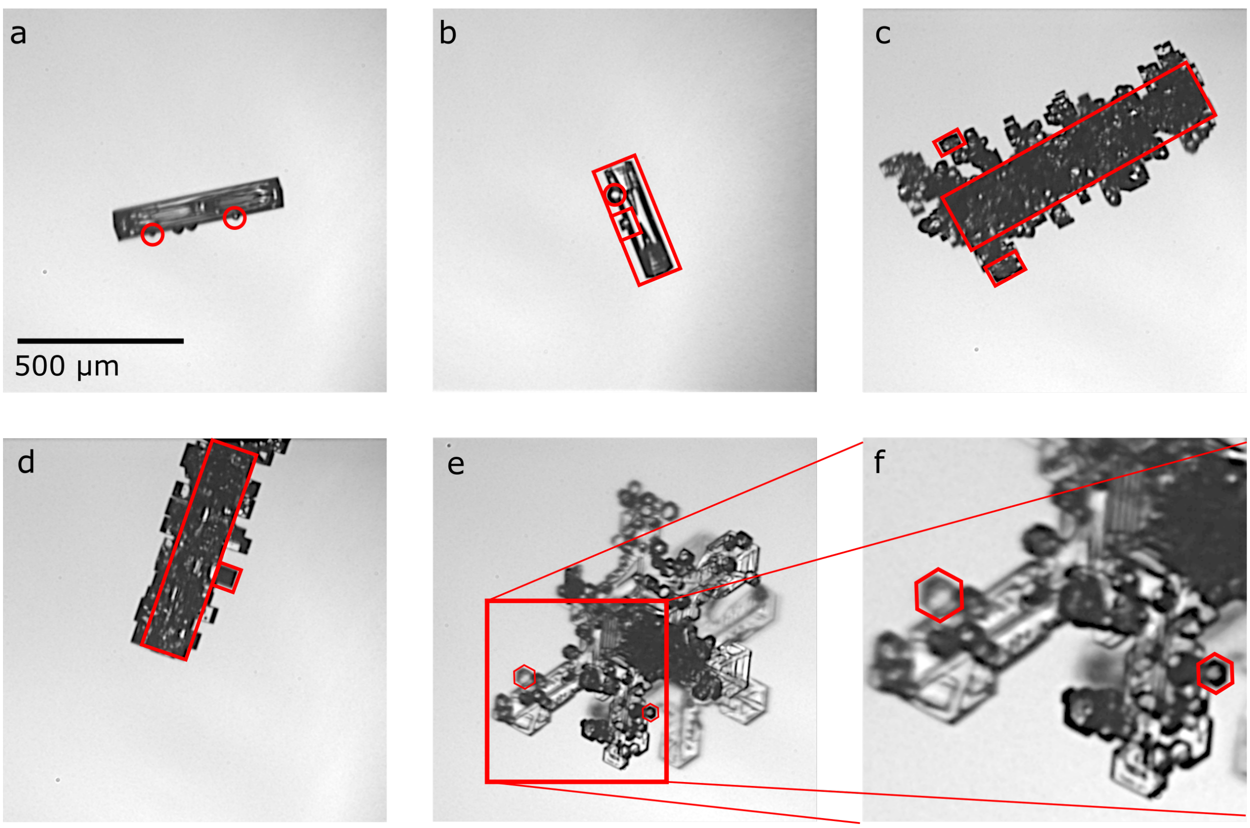

FIG. 8. Exemplary rimed ice particles sampled during the IMPACTS campaign: slightly, "normally rimed" column (a), slightly rimed column with both normal and epitaxial riming (b), heavily epitaxially rimed columns (c,d) and a moderately, epitaxially rimed plate (e).

Multiple studies exist investigating the orientation of crystallographic axes of the freezing of rime particles, both in-vitro (Magono and Aburakawa 1969; Takahashi 1979; Mizuno 1984; Mizuno and Wakahama 1983) and in-situ (Uyeda and Kikuchi 1980). It has been shown that the crystal structure of rimed (still round) droplets matches the underlying lattice structure. At high temperatures $-10 \leq T \leq 0$°C, most small droplets (D $\lesssim$40 μm) freeze as single crystals whereas at lower temperatures (T ≤ -15°C), rime particles tend to freeze as polycrystals. However, to our knowledge, so far no studies exist that analyze the properties and formation conditions of the aforementioned epitaxially rimed particles. In the following, we present detailed observations of such ice particles and propose that they are the result of vapor deposition on rimed particles.

a. Correlation of Epitaxial Riming with Ambient Conditions

In Fig. 9, we show the relative occurrence of normally and epitaxially rimed particles during the ACLOUD and SOCRATES campaigns as related with ambient microphysical parameters. The corresponding fit parameters for all histograms are shown in Tab. 2. Again, only particles sampled at a temperature T ≥ -17°C with diameter D $\geq$ 100 μm that were distinctively classified according to the aforementioned manual classification are included.

Fig. 9a shows that there is a tendency to find more epitaxial riming at higher temperatures near T = 0°C, where up to almost 40% of all rimed particles show epitaxial riming ($R^2 = 0.93$). Between -5 and -10°C, the fraction of epitaxial riming slightly decreases from 40% to 30%. Below T < -10°C, the percentage of epitaxial riming decreases below 20%, although it should be noted that the statistics for this temperature region are weak. This temperature dependency is in accordance with the aforementioned studies showing that the rime particles tend to freeze as single crystals along the c-axis of the underlying particle.

Fig. 9b shows a slight relation of the occurrence of epitaxial particles with the size of the underlying particle. For small particles below D $\leq$ 150 μm, the fraction of epitaxially rimed particles is 20%. This increases to up to 40% for ice particles larger than D $\geq$ 300 μm. For larger particles, the fraction of epitaxially rimed crystals is only weakly dependent on particle size. The relation of particle size with the presence of epitaxial riming can be explained by the fact that epitaxial riming is caused by vapor deposition during the ageing process of rimed particles, which naturally also causes the particle to grow on their main surfaces.

Figs. 9c and d show a trend of increasing fraction of epitaxially rimed particles with positive (upward) Doppler velocity, indicating a relationship with updrafts. We see no substantial differ-

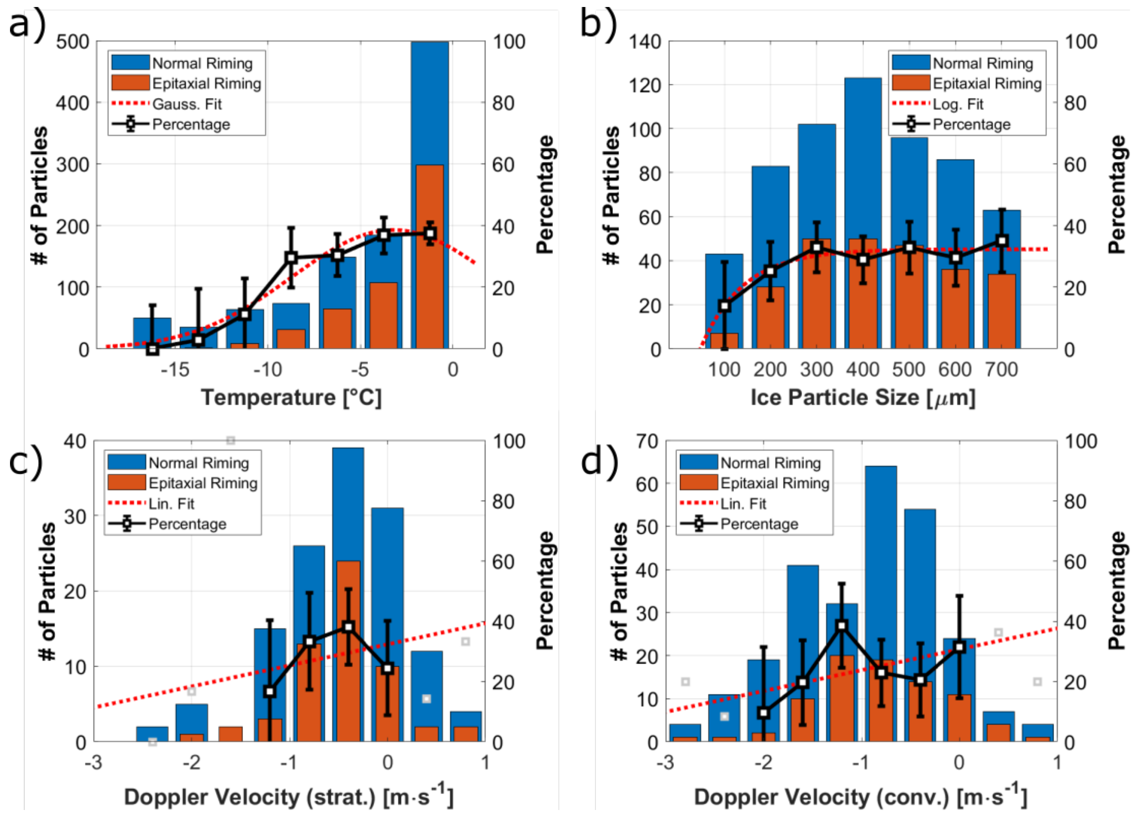

FIG. 9. Absolute number of analyzed particles for normal (blue) and epitaxial (red) riming and fraction of epitaxially rimed particles as a function of ambient temperature (a), ice particle size (b) and HCR Doppler velocity for statiform (c) and convective cloud segments (d). Only bins with more than $n \geq 20$ data points were taken into account (n<20 are shown in grey).

ence between the stratiform and convective cases. Again, comparisons with LWC and the other previously discussed parameters show no significant relationship (plots shown in the SI).

Next, we will present a case study of a MPC sampled during the IMPACTS campaign. We investigate the assumption that the ice particles with epitaxial riming are the result of ageing of rimed particles and discuss its formation process.

TABLE 2. Fit parameters to the riming percentage histograms shown in Fig. 9.

		Fit function	R^2
Temperature		$y = -0.312\ x^2 + -1.37\ x + 36.6$	0.930
Ice particle diameter	(PHIPS)	$y = 32.3 - \exp[-109\ (x-367)]$	0.898
Vertical Doppler velocity	(HCR, strat.)	$y = 6.98\ x + 32.3$	0.144
Vertical Doppler velocity	(HCR, conv.)	$y = 6.92\ x + 30.7$	0.265

b. Case Study Feb01st - Epitaxial Riming on Columns

Fig. 10 shows microphysical data collected on February 1st during the 2020 IMPACTS campaign. The MPC segment discussed in this case study was probed from 12:42:30 - 12:49:00 UTC (Δt = 06:30 min, which corresponds to Δs = 58.5 km) at an altitude of approximately 4,300 m and a temperature of about -12°C around 36°N/73°W, roughly 300 km off the US east coast. The vertical wind velocity was at a constant value around ± 0 m s^{-1}. The relative humidity with respect to water averaged about 93%. The liquid water content (LWC) measured with the CDP averaged around 0.1 g m^{-3} and the total water content (TWC) measured with the 2DS was around 0.5 g m^{-3}. The number-weighed mean particle diameter was around 20 µm for droplets and between 200 to 800 µm for ice particles based on the measurements of CDP and 2DS, respectively.

The trigger threshold of PHIPS was set in a way that the instrument started to trigger on droplets with diameters larger than D > 100 µm. In this segment, in total, 1,589 particles were triggered and 575 stereo images were acquired. Examples of micrographs of particles from this flight segment are shown in Fig. 11. Of the 575 stereo images, 259 (45%) were not classified since they were identified as potential shattering fragments smaller than D = 100 µm. Shattering artifacts can be identified from the PHIPS stereo images that have a field of view of approx. 2.19 mm x 1.65 mm by looking for satellite particles. Shattering fragments do not always appear as “satellites” but can be found as single fragments within the image frame. Such individual shattering fragments can be typically identified as having sharp edges and a shape that does not appear to resemble that of a typical vapor grown crystal (i.e. a lack of hexagonal symmetry of the crystal facets). If such particles were identified during the manual image inspection, they were also categorized as shattering cases. Of the remaining ice particles (320) most are classified as columnar particles (173) and needles (33). These particles show a wide spectrum of riming degree, ranging from unrimed (43) to slightly (44), moderately (42) and heavily rimed particles (124). We see different "types" of riming: most are epitaxially rimed (87), while 56 show normal riming. Furthermore, we see numerous particles with evidence of both normal and epitaxial riming on the same particle (20), which we refer to as *mixed riming* in the following. Apart from that, we see the presence of 3 large drizzle droplets with diameters 200-300 µm as well as rimed dendrites (30) and graupel (48) particles. 35 particles were classified as irregulars. Similar particle shapes are observed on the CPI imagery (not shown here).

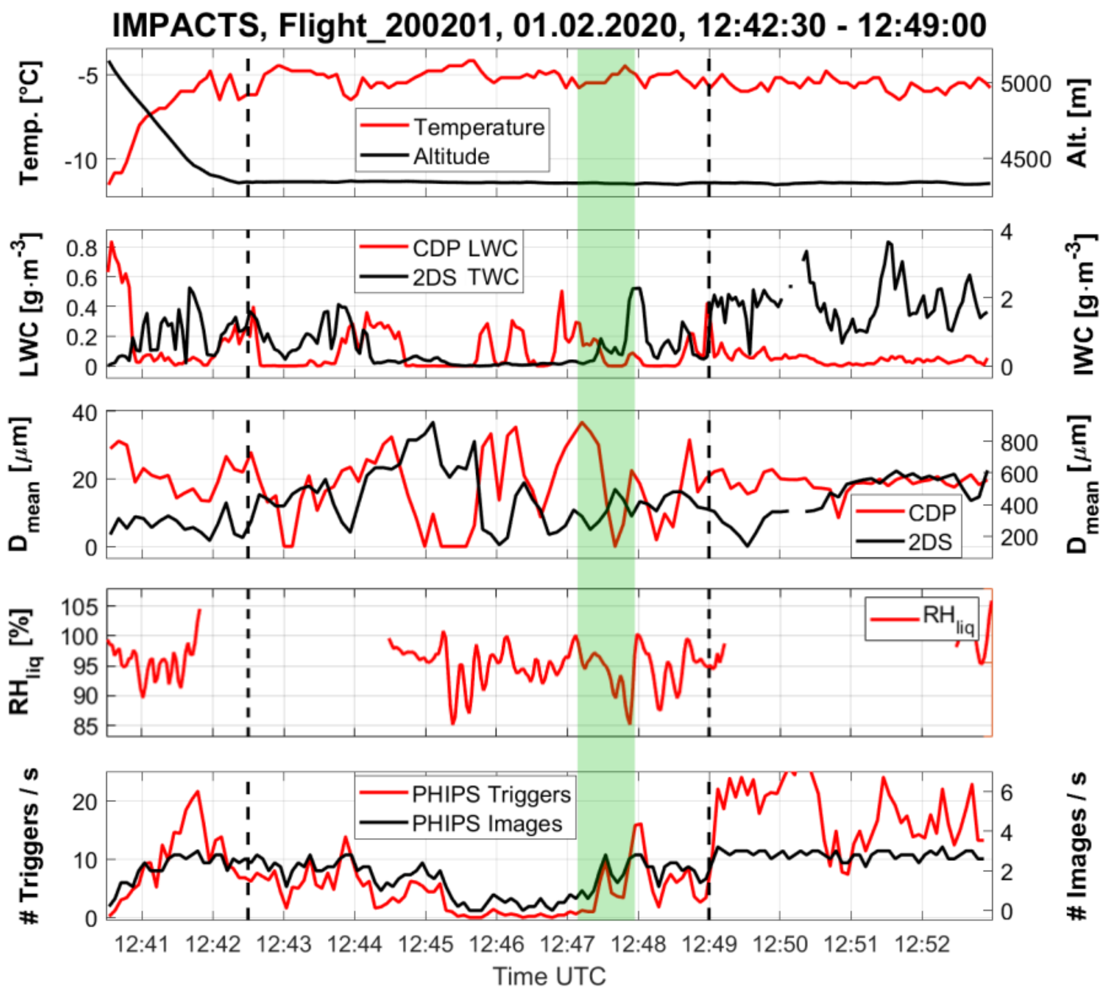

FIG. 10. Example of PHIPS data acquired in a mixed-phase cloud near the US east coast sampled during the IMPACTS campaign on February 1st, 2020. The graph shows an overview of temperature, altitude, CDP liquid water content, 2DS total water content, CDP and 2DS number-weighed mean particle diameter and number of PHIPS images and total triggers. Corresponding representative PHIPS images of particles sampled during this segment are shown in Fig. 11 The green shaded area marks a 45 s segment during which the four particles shown in Fig. 12 were acquired.

The lower panel of Fig. 12 shows four exemplary ice particles that were sampled within a 45 s window (12:47:07 - 12:47:52 UTC, corresponding to a distance of 6.7 km) that is indicated by the shaded green area in Fig. 10. The particles that were sampled within this period show columnar particles during different stages of the riming process: an unrimed (a), a normally rimed (b), a

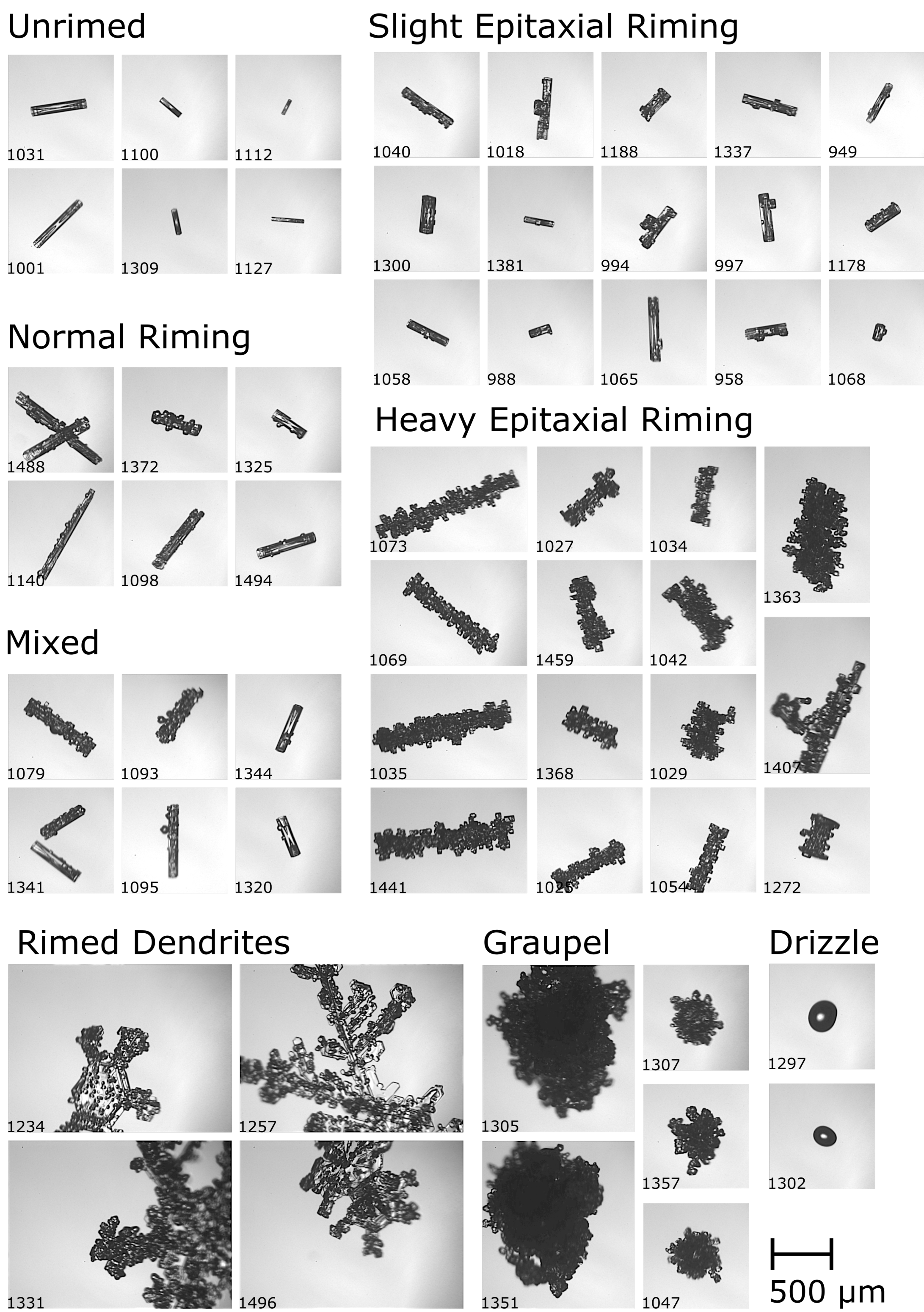

FIG. 11. Corresponding representative PHIPS images of particles sampled during the segment indicated by the dashed black lines in in Fig. 10. The numbers in the bottom left denote the image number.

mixed rimed (c) and epitaxially rimed column (d). Since we observe normal and epitaxial riming not only within the same segment in near spatial vicinity, but also on the same singular particles, we argue that normal and epitaxial riming are, as hypothesized, interlinked. As proposed by Korolev et al. (2020), we argue that epitaxial riming is the result of the ageing (deposition growth) of normally rimed particles as sketched in the upper panel of Fig. 12: An unrimed ice particle (a) accretes a supercooled droplet and forms the initial primary "normal" riming (b). Ambient water vapour deposits on the rime matching the lattice structure of the underlying particle and thus forming the faceted surface. More droplets are accreted such that normal and epitaxial riming can be observed on the same particle (c). The process repeats and the particle grows further until, eventually, the whole surface is covered by epitaxial rime (d).

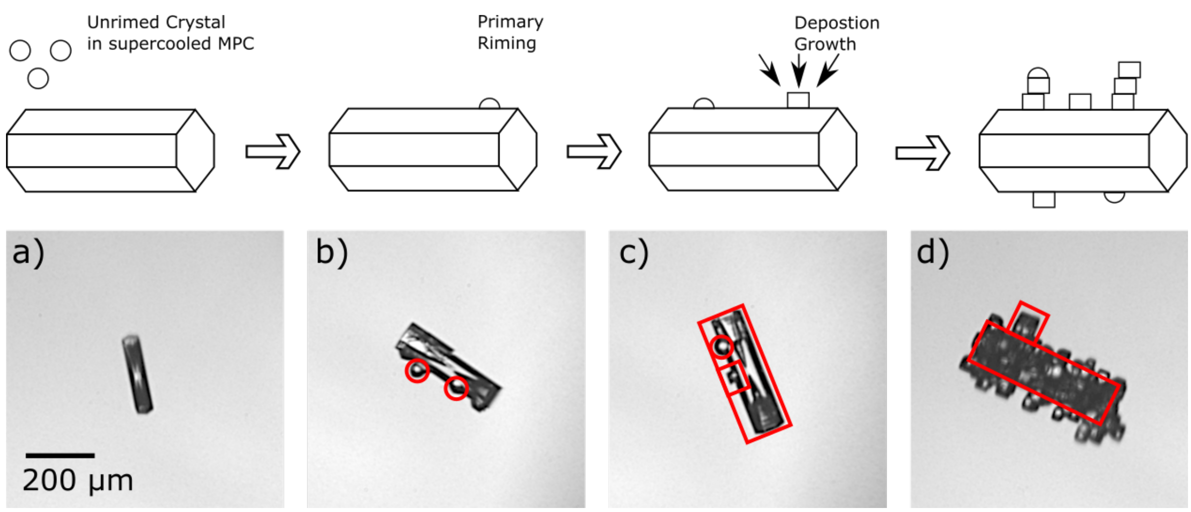

FIG. 12. Schematic sketch of an epitaxially rimed column during different stages of the ageing process: unrimed (a), normally rimed (b), mixed (c), and epitaxially rimed column (d). The lower panel shows corresponding exemplary PHIPS images (#1309, #1325, #1320, and #1368) acquired within a 45 s segment in the presented case-study (shaded green area in Fig. 10).

5. Summary and Conclusion

In this work, we have presented in-situ observations using the PHIPS probe during three aircraft campaigns targeting MPCs in the Arctic, the Southern Ocean and US east coast. We have shown that riming is prevalent in the sampled clouds. We have manually classified ice particles in a size range from $100 \leq D \leq 700\,\mu m$ and in the temperature range between $-17°C \leq T \leq 0°C$ regarding their riming status (rimed or unrimed) and surface riming degree (SRD). We show that riming is most prevalent at temperatures around -7°C, where, on average, 43% of the investigated particles showed evidence of riming. We show that riming fraction increases with ice particle size (<20% for D ≤200 µm, 35-40% for D ≤400 µm) and liquid water content (25% for LWC ≤ 0.05 g m^{-3}, up to 60% for LWC = 0.5 g m^{-3}).

We investigated riming features such as surface riming degree, size of rime particles and one-sided riming based on visual inspection of individual stereo-images of ice crystals imaged by PHIPS during these campaigns. We show that the surface riming degree increases with decreasing temperature and increasing ice particle size.

Furthermore, we have described ice particles with faceted, crystalline build-up that is aligned to the lattice structure of the underlying particle. We call this "epitaxial riming" that we differentiate from the round "normal riming". Epitaxial riming is most notable in the temperature range from -10°C≤ T ≤0°C where epitaxial riming is visible on 32-37% of all rimed particles. We have presented a case study that demonstrates that normal and epitaxial riming can be observed in the same cloud segments and even simultaneously on the same single ice particles. We argue that epitaxially rimed particles are the result of deposition growth of water vapor on primarily rimed particles during their ageing process. However, further studies are needed to investigate the exact growth mechanisms of epitaxial riming, for example in laboratory studies. Furthermore, implications of epitaxial riming are still unclear. For example, it is unclear if epitaxial riming affects the rime splintering process and the splinter production rate.

Currently, the implications of riming towards the climate are not yet well understood as most present day climate prediction models lack a parameterization of riming and consider riming only for large particles (D ≥ 1 mm) in the sense of graupel and snow. Riming on smaller particles is usually not considered. The presented correlation between riming fraction and ambient microphysical parameters can be used as a basis for first steps towards such a riming parameterization for small or large scale models.

Acknowledgments. We express our gratitude all participants of the field studies for their efforts, in particular the technical crew of the AWI Polar 6, NSF G-V and NASA P3. We would like to acknowledge operational, technical and scientific support provided by NCAR's Earth Observing Laboratory, sponsored by the National Science Foundation. We thank Ulrike Romatschke for her valuable help with the HCR data. We would also like to thank the technical and scientific staff of IMK-AAF for their continuous support. We also thank Alexei Korolev and an anonymous reviewer who provided valuable feedback feedback that improved and clarified the manuscript. This work has received funding from the Helmholtz Research Program Atmosphere and Climate, by the German Research Foundation (DFG grants JA 2818/1-1 and SCHN 1140/3-1) and the Helmholtz Association's Initiative and Networking Fund (grant agreement no. VH-NG-1531).

Data availability statement. The PHIPS single particle scattering data can be found online in the PANGEA database (`https://doi.org/10.1594/PANGAEA.902611`) for ACLOUD and the EOL database (`https://doi.org/10.5065/D6639NKQ`) for SOCRATES. The single particle microscopic stereo images from those two campaigns are available upon request from the authors. The single particle microscopic stereo images from the IMPACTS campaign can be found in the GHVR DAAC database (`http://dx.doi.org/10.5067/IMPACTS/PHIPS/DATA101`)

References

Abdelmonem, A., E. Järvinen, D. Duft, E. Hirst, S. Vogt, T. Leisner, and M. Schnaiter, 2016: Phips–halo: the airborne particle habit imaging and polar scattering probe – part 1: Design and operation. *Atmospheric Measurement Techniques*, **9 (7)**, 3131–3144, https://doi.org/10.5194/amt-9-3131-2016, URL https://www.atmos-meas-tech.net/9/3131/2016/.

Baltensperger, U., M. Schwikowski, D. Jost, S. Nyeki, H. Gäggeler, and O. Poulida, 1998: Scavenging of atmospheric constituents in mixed phase clouds at the high-alpine site jungfraujoch part i: Basic concept and aerosol scavenging by clouds. *Atmospheric Environment*, **32 (23)**, 3975–3983, https://doi.org/https://doi.org/10.1016/S1352-2310(98)00051-X, URL https://www.sciencedirect.com/science/article/pii/S135223109800051X.

Blahak, U., and A. Seifert, 2015: Cosmo / clm / art training course, langen, march 2015. URL https://www.hzg.de/imperia/md/assets/clm/neu5_tl3.pdf.

Bruintjes, R. T., A. J. Heymsfield, and T. W. Krauss, 1987: An examination of double-plate ice crystals and the initiation of precipitation in continental cumulus clouds. *Journal of Atmospheric Sciences*, **44 (9)**, 1331 – 1350, https://doi.org/10.1175/1520-0469(1987)044<1331:AEODPI>2.0.

CO;2, URL https://journals.ametsoc.org/view/journals/atsc/44/9/1520-0469_1987_044_1331_aeodpi_2_0_co_2.xml.

Bryant, G., J. Hallett, and B. Mason, 1960: The epitaxial growth of ice on single-crystalline substrates. *Journal of Physics and Chemistry of Solids*, **12 (2)**, 189–IN18, https://doi.org/https://doi.org/10.1016/0022-3697(60)90036-6, URL https://www.sciencedirect.com/science/article/pii/0022369760900366.

Diao, M., 2021: Vcsel 25hz water vapor data. version 2.0. UCAR/NCAR - Earth Observing Laboratory, URL https://data.eol.ucar.edu/dataset/552.052, https://doi.org/10.26023/V925-2H41-SD0F.

Ehrlich, A., and Coauthors, 2019: Collection of data sources for the Arctic CLoud Observations Using airborne measurements during polar Day (ACLOUD) campaign, North-West of Svalbard between 23 May - 26 June 2017. PANGAEA, URL https://doi.org/10.1594/PANGAEA.902603, https://doi.org/10.1594/PANGAEA.902603.

EOL, 2018: Socrates: Southern ocean clouds radiation aerosol transport experimental study. UCAR/NCAR - Earth Observing Laboratory, URL https://data.eol.ucar.edu/project/SOCRATES.

Fan, J., S. Ghan, M. Ovchinnikov, X. Liu, P. J. Rasch, and A. Korolev, 2011: Representation of arctic mixed-phase clouds and the wegener-bergeron-findeisen process in climate models: Perspectives from a cloud-resolving study. *Journal of Geophysical Research: Atmospheres*, **116 (D1)**, https://doi.org/https://doi.org/10.1029/2010JD015375, URL https://agupubs.onlinelibrary.wiley.com/doi/abs/10.1029/2010JD015375, https://agupubs.onlinelibrary.wiley.com/doi/pdf/10.1029/2010JD015375.

Field, P. R., and Coauthors, 2017: *Secondary Ice Production - current state of the science and recommendations for the future*, Meteorological Monographs, Vol. 58, 7.1–7.20. American Meteorological Society, Boston (MA), https://doi.org/10.1175/AMSMONOGRAPHS-D-16-0014.1, 12.01.01; LK 01.

Garrett, T. J., and S. E. Yuter, 2014: Observed influence of riming, temperature, and turbulence on the fallspeed of solid precipitation. *Geophysical Research Letters*, **41 (18)**, 6515–6522, https://doi.org/https://doi.org/10.1002/2014GL061016, URL https://agupubs.onlinelibrary.wiley.com/doi/abs/10.1002/2014GL061016, https://agupubs.onlinelibrary.wiley.com/doi/pdf/10.1002/2014GL061016.

Hallett, J., and S. C. Mossop, 1974: Production of secondary ice particles during the riming process. *Nature*, **249 (5452)**, 26–28, https://doi.org/https://doi.org/10.1038/249026a0, URL https://rmets.onlinelibrary.wiley.com/doi/abs/10.1002/qj.49710042514, https://rmets.onlinelibrary.wiley.com/doi/pdf/10.1002/qj.49710042514.

Harimaya, T., 1975: The riming properties of snow crystals. *Journal of the Meteorological Society of Japan. Ser. II*, **53 (6)**, 384–392, https://doi.org/10.2151/jmsj1965.53.6_384.

Hegg, D. A., A. D. Clarke, S. J. Doherty, and J. Ström, 2011: Measurements of black carbon aerosol washout ratio on svalbard. *Tellus B*, **63 (5)**, 891–900, https://doi.org/https://doi.org/10.1111/j.1600-0889.2011.00577.x, URL https://onlinelibrary.wiley.com/doi/abs/10.1111/j.1600-0889.2011.00577.x, https://onlinelibrary.wiley.com/doi/pdf/10.1111/j.1600-0889.2011.00577.x.

Herzegh, P. H., and P. V. Hobbs, 1980: The mesoscale and microscale structure and organization of clouds and precipitation in midlatitude cyclones. ii: Warm-frontal clouds. *Journal of Atmospheric Sciences*, **37 (3)**, 597 – 611, https://doi.org/10.1175/1520-0469(1980)037<0597:TMAMSA>2.0.CO;2, URL https://journals.ametsoc.org/view/journals/atsc/37/3/1520-0469_1980_037_0597_tmamsa_2_0_co_2.xml.

Järvinen, E., and Coauthors, 2018: Additional global climate cooling by clouds due to ice crystal complexity. *Atmospheric Chemistry and Physics*, **18 (21)**, 15 767–15 781, https://doi.org/10.5194/acp-18-15767-2018, URL https://www.atmos-chem-phys.net/18/15767/2018/.

Järvinen, E., and Coauthors, 2021: Ice crystal complexity and link to cirrus cloud radiative effect. *Journal of Geophysical Research: Atmospheres*, **2021**, in review.

Keppas, S. C., J. Crosier, T. W. Choularton, and K. N. Bower, 2017: Ice lollies: An ice particle generated in supercooled conveyor belts. *Geophysical Research Letters*, **44 (10)**, 5222–5230, https://doi.org/https://doi.org/10.1002/2017GL073441, URL https://agupubs.onlinelibrary.wiley.com/doi/abs/10.1002/2017GL073441, https://agupubs.onlinelibrary.wiley.com/doi/pdf/10.1002/2017GL073441.

Khain, A., A. Pokrovsky, and I. Sednev, 1999: Some effects of cloud–aerosol interaction on cloud microphysics structure and precipitation formation: numerical experiments with a spectral microphysics cloud ensemble model. *Atmospheric Research*, **52 (3)**, 195–220, https://doi.org/https://doi.org/10.1016/S0169-8095(99)00027-7, URL https://www.sciencedirect.com/science/article/pii/S0169809599000277.

Kikuchi, K., and H. Uyeda, 1979: Cloud droplets and rain drops collected and frozen on natural snow crystals. *Journal of the Meteorological Society of Japan. Ser. II*, **57 (3)**, 273–281, https://doi.org/10.2151/jmsj1965.57.3_273.

Kiselev, A., F. Bachmann, P. Pedevilla, S. J. Cox, A. Michaelides, D. Gerthsen, and T. Leisner, 2016: Active sites in heterogeneous ice nucleation—the example of k-rich feldspars. *Science*, https://doi.org/10.1126/science.aai8034, URL https://science.sciencemag.org/content/early/2016/12/07/science.aai8034, https://science.sciencemag.org/content/early/2016/12/07/science.aai8034.full.pdf.

Kneifel, S., and D. Moisseev, 2020: Long-term statistics of riming in nonconvective clouds derived from ground-based doppler cloud radar observations. *Journal of the Atmospheric Sciences*, **77 (10)**, 3495 – 3508, https://doi.org/10.1175/JAS-D-20-0007.1, URL https://journals.ametsoc.org/view/journals/atsc/77/10/jasD200007.xml.

Knudsen, E. M., and Coauthors, 2018: Meteorological conditions during the acloud/pascal field campaign near svalbard in early summer 2017. *Atmospheric Chemistry and Physics*, **18 (24)**, 17 995–18 022, https://doi.org/10.5194/acp-18-17995-2018, URL https://www.atmos-chem-phys.net/18/17995/2018/.

Korolev, A., and Coauthors, 2017: Mixed-phase clouds: Progress and challenges. *Meteorological Monographs*, **58**, 5.1–5.50, https://doi.org/10.1175/AMSMONOGRAPHS-D-17-0001.1, URL https://doi.org/10.1175/AMSMONOGRAPHS-D-17-0001.1, https://doi.org/10.1175/AMSMONOGRAPHS-D-17-0001.1.

Korolev, A., and Coauthors, 2020: A new look at the environmental conditions favorable to secondary ice production. *Atmospheric Chemistry and Physics*, **20 (3)**, 1391–1429, https://doi.org/10.5194/acp-20-1391-2020, URL https://acp.copernicus.org/articles/20/1391/2020/.

Leinonen, J., and W. Szyrmer, 2015: Radar signatures of snowflake riming: A modeling study. *Earth and Space Science*, **2 (8)**, 346–358, https://doi.org/https://doi.org/10.1002/2015EA000102, URL https://agupubs.onlinelibrary.wiley.com/doi/abs/10.1002/2015EA000102, https://agupubs.onlinelibrary.wiley.com/doi/pdf/10.1002/2015EA000102.

Leinonen, J., and Coauthors, 2018: Retrieval of snowflake microphysical properties from multifrequency radar observations. *Atmospheric Measurement Techniques*, **11 (10)**, 5471–5488, https://doi.org/10.5194/amt-11-5471-2018, URL https://amt.copernicus.org/articles/11/5471/2018/.

Libbrecht, K., 2016: *Ken Libbrecht's Field Guide to Snowflakes*. Voyageur Press, URL https://books.google.de/books?id=eOv83aUgOvwC.

Libbrecht, K., C. Miller, R. Potter, N. Budaeva, C. Lemon, and S. Thomas, 2015: Toward a comprehensive model of snow crystal growth: 4. measurements of diffusion-limited growth at -15 c.

Lin, Y., L. Donner, and B. Colle, 2011: Parameterization of riming intensity and its impact on ice fall speed using arm data. *Monthly Weather Review - MON WEATHER REV*, **139**, 1036–1047, https://doi.org/10.1175/2010MWR3299.1.

Locatelli, J. D., and P. V. Hobbs, 1974: Fall speeds and masses of solid precipitation particles. *Journal of Geophysical Research (1896-1977)*, **79 (15)**, 2185–2197, https://doi.org/https://doi.org/10.1029/JC079i015p02185, URL https://agupubs.onlinelibrary.wiley.com/doi/abs/10.1029/JC079i015p02185, https://agupubs.onlinelibrary.wiley.com/doi/pdf/10.1029/JC079i015p02185.

Magono, C., and H. Aburakawa, 1969: Expermental studies on snow crystals of plane type with spatial branches. *Journal of the Faculty of Science, Hokkaido University. Series 7, Geophysics*, **3 (2)**, 85–97, URL http://hdl.handle.net/2115/8680.

Magono, C., and C. W. Lee, 1966: Meteorological classification of natural snow crystals. *Journal of the Faculty of Science, Hokkaido University. Series 7, Geophysics*, **2 (4)**, 321–335, URL http://hdl.handle.net/2115/8672.

Martin, M. Y., and R. Bennett, 2020: P-3 meteorological and navigation data impacts. NASA Global Hydrometeorology Resource Center DAAC, URL https://ghrc.nsstc.nasa.gov/hydro/details/p3metnavimpacts, https://doi.org/10.5067/IMPACTS/P3/DATA101.

Mason, S. L., C. J. Chiu, R. J. Hogan, D. Moisseev, and S. Kneifel, 2018: Retrievals of riming and snow density from vertically pointing doppler radars. *Journal of Geophysical Research: Atmospheres*, **123 (24)**, 13,807–13,834, https://doi.org/https://doi.org/10.1029/2018JD028603, URL https://agupubs.onlinelibrary.wiley.com/doi/abs/10.1029/2018JD028603, https://agupubs.onlinelibrary.wiley.com/doi/pdf/10.1029/2018JD028603.

McCoy, D. T., I. Tan, D. L. Hartmann, M. D. Zelinka, and T. Storelvmo, 2016: On the relationships among cloud cover, mixed-phase partitioning, and planetary albedo in gcms. *Journal of Advances in Modeling Earth Systems*, **8 (2)**, 650–668, https://doi.org/10.1002/2015MS000589, URL https://agupubs.onlinelibrary.wiley.com/doi/abs/10.1002/2015MS000589, https://agupubs.onlinelibrary.wiley.com/doi/pdf/10.1002/2015MS000589.

McFarquhar, G. M., and Coauthors, 2019: Airborne, ship-, and ground-based observations of clouds, aerosols, and precipitation from recent field projects over the southern ocean. *99th annual meeting, American Meteorological Society*, URL https://ams.confex.com/ams/2019Annual/meetingapp.cgi/Paper/350863.

McMurdie, L., G. Heymsfield, J. Yorks, and S. Braun, 2019: Investigation of microphysics and precipitation for atlantic coast-threatening snowstorms (impacts) collection. NASA EOSDIS Global Hydrology Resource Center Distributed, Active Archive Center, Huntsville, Alabama, U.S.A., URL http://dx.doi.org/10.5067/IMPACTS/DATA101.

Mizuno, Y., 1984: Epitaxial freezing of supercooled droplets on ice surfaces. *Contributions from the Institute of Low Temperature Science*, **A33**, 1–27, URL http://hdl.handle.net/2115/20248.

Mizuno, Y., and G. Wakahama, 1983: Structure and orientation of frozen droplets on ice surfaces. *The Journal of Physical Chemistry*, **87 (21)**, 4161–4167, https://doi.org/10.1021/j100244a037, URL https://doi.org/10.1021/j100244a037, https://doi.org/10.1021/j100244a037.

Mosimann, L., 1995: An improved method for determining the degree of snow crystal riming by vertical doppler radar. *Atmospheric Research*, **37 (4)**, 305–323, https://doi.org/https://doi.org/10.1016/0169-8095(94)00050-N, URL https://www.sciencedirect.com/science/article/pii/016980959400050N.

Mosimann, L., M. Steiner, J. Collett, and et al., 1993: Ice crystal observations and the degree of riming in winter precipitation. *Water Air Soil Pollution*, **68**, 29–42, https://doi.org/https://doi.org/10.1007/BF00479391.

Mosimann, L., E. Weingartner, and A. Waldvogel, 1994: An analysis of accreted drop sizes and mass on rimed snow crystals. *Journal of Atmospheric Sciences*, **51 (11)**, 1548 – 1558, https://doi.org/10.1175/1520-0469(1994)051<1548:AAOADS>2.0.CO;2, URL https://journals.ametsoc.org/view/journals/atsc/51/11/1520-0469_1994_051_1548_aaoads_2_0_co_2.xml.

Ono, A., 1969: The shape and riming properties of ice crystals in natural clouds. *Journal of Atmospheric Sciences*, **26 (1)**, 138 – 147, https://doi.org/10.1175/1520-0469(1969)026<0138:TSARPO>2.0.CO;2, URL https://journals.ametsoc.org/view/journals/atsc/26/1/1520-0469_1969_026_0138_tsarpo_2_0_co_2.xml.

Ovchinnikov, M., and Coauthors, 2014: Intercomparison of large-eddy simulations of arctic mixed-phase clouds: Importance of ice size distribution assumptions. *Journal of Advances in Modeling Earth Systems*, **6 (1)**, 223–248, https://doi.org/https://doi.org/10.1002/2013MS000282, URL https://agupubs.onlinelibrary.wiley.com/doi/abs/10.1002/2013MS000282, https://agupubs.onlinelibrary.wiley.com/doi/pdf/10.1002/2013MS000282.

Pashley, D., 1956: The study of epitaxy in thin surface films. *Advances in Physics*, **5 (18)**, 173–240, https://doi.org/10.1080/00018735600101175, URL https://doi.org/10.1080/00018735600101175, https://doi.org/10.1080/00018735600101175.

Pflaum, J. C., and H. R. Pruppacher, 1979: A wind tunnel investigation of the growth of graupel initiated from frozen drops. *Journal of Atmospheric Sciences*, **36 (4)**, 680 – 689, https://doi.org/10.1175/1520-0469(1979)036<0680:AWTIOT>2.0.CO;2, URL https://journals.ametsoc.org/view/journals/atsc/36/4/1520-0469_1979_036_0680_awtiot_2_0_co_2.xml.

Rango, A., J. Foster, E. G. Josberger, E. F. Erbe, W. P. Wergin, and C. Pooley, 2003: Rime and graupel: Description and characterization as revealed by low-temperature scanning electron microscopy. *Scanning*, **25 (3)**, 121–131, https://doi.org/https://doi.org/10.1002/sca.4950250304, URL https://onlinelibrary.wiley.com/doi/abs/10.1002/sca.4950250304, https://onlinelibrary.wiley.com/doi/pdf/10.1002/sca.4950250304.

Romatschke, U., 2021: Melting layer detection and observation with the ncar airborne w-band radar. *Remote Sensing*, **13 (9)**, https://doi.org/10.3390/rs13091660, URL https://www.mdpi.com/2072-4292/13/9/1660.

Romatschke, U., and M. Dixon, 2022: Vertically resolved convective/stratiform echo type identification and convectivity retrieval for vertically pointing radars. https://doi.org/10.31223/x54s77, URL https://doi.org/10.31223/x54s77.

Saleeby, S. M., and W. R. Cotton, 2008: A binned approach to cloud-droplet riming implemented in a bulk microphysics model. *Journal of Applied Meteorology and Climatology*, **47 (2)**, 694 – 703, https://doi.org/10.1175/2007JAMC1664.1, URL https://journals.ametsoc.org/view/journals/apme/47/2/2007jamc1664.1.xml.

Schnaiter, M., E. Järvinen, A. Abdelmonem, and T. Leisner, 2018: Phips-halo: the airborne particle habit imaging and polar scattering probe – part 2: Characterization and first results. *Atmospheric Measurement Techniques*, **11 (1)**, 341–357, https://doi.org/10.5194/amt-11-341-2018, URL https://www.atmos-meas-tech.net/11/341/2018/.

Schnaiter, M., and Coauthors, 2016: Cloud chamber experiments on the origin of ice crystal complexity in cirrus clouds. *Atmospheric Chemistry and Physics*, **16 (8)**, 5091–5110, https://doi.org/10.5194/acp-16-5091-2016, URL https://acp.copernicus.org/articles/16/5091/2016/.

Schön, R., and Coauthors, 2011: Particle habit imaging using incoherent light: A first step toward a novel instrument for cloud microphysics. *Journal of Atmospheric and Oceanic Technology*, **28 (4)**, 493–512, https://doi.org/10.1175/2011JTECHA1445.1, URL https://doi.org/10.1175/2011JTECHA1445.1, https://doi.org/10.1175/2011JTECHA1445.1.

Stevens, R. G., and Coauthors, 2018: A model intercomparison of ccn-limited tenuous clouds in the high arctic. *Atmospheric Chemistry and Physics*, **18 (15)**, 11 041–11 071, https://doi.org/10.5194/acp-18-11041-2018, URL https://acp.copernicus.org/articles/18/11041/2018/.

Takahashi, C., 1979: Formation of poly-crystalline snow crystals by riming process. *Journal of the Meteorological Society of Japan. Ser. II*, **57 (5)**, 458–464, https://doi.org/10.2151/jmsj1965.57.5_458.

UCAR/NCAR-Earth Observing Laboratory, 2019: Socrates: Low rate (lrt - 1 sps) navigation, state parameter, and microphysics flight-level data. version 1.3. UCAR/NCAR - Earth Observing Laboratory, URL https://data.eol.ucar.edu/dataset/552.002, https://doi.org/10.5065/D6M32TM9.

UCAR/NCAR-EOL, 2022: Ncar hcr radar and hsrl lidar moments data. version 3.0. ucar/ncar - earth observing laboratory. URL https://doi.org/10.5065/D68914PH.

Uyeda, H., and K. Kikuchi, 1978: Freezing experiment of supercooled water droplets frozen by using single crystal ice. *Journal of the Meteorological Society of Japan. Ser. II*, **56 (1)**, 43–51, https://doi.org/10.2151/jmsj1965.56.1_43.

Uyeda, H., and K. Kikuchi, 1980: Measurements of the principal axis of frozen hemispheric water droplets. *Journal of the Meteorological Society of Japan. Ser. II*, **58 (1)**, 52–58, https://doi.org/10.2151/jmsj1965.58.1_52.

Waitz, F., M. Schnaiter, T. Leisner, and E. Järvinen, 2021: Phips-halo: the airborne particle habit imaging and polar scattering probe – part 3: Single particle phase discrimination and particle size distribution based on angular scattering function. *Atmospheric Measurement Techniques Discussions*, **2021**, 1–28, https://doi.org/10.5194/amt-2020-297, URL https://amt.copernicus.org/preprints/amt-2020-297/.

Wang, P. K., and W. Ji, 2000: Collision efficiencies of ice crystals at low–intermediate reynolds numbers colliding with supercooled cloud droplets: A numerical study. *Journal of the Atmospheric Sciences*, **57 (8)**, 1001 – 1009, https://doi.org/10.1175/1520-0469(2000)057<1001:CEOICA>2.0.CO;2, URL https://journals.ametsoc.org/view/journals/atsc/57/8/1520-0469_2000_057_1001_ceoica_2.0.co_2.xml.

Wendisch, M., A. Macke, A. Ehrlich, C. Lüpkes, and Coauthors, 2019: The arctic cloud puzzle: Using acloud/pascal multiplatform observations to unravel the role of clouds and aerosol particles in arctic amplification. *Bulletin of the American Meteorological Society*, **100 (5)**, 841–871, https://doi.org/10.1175/BAMS-D-18-0072.1, URL https://doi.org/10.1175/BAMS-D-18-0072.1, https://doi.org/10.1175/BAMS-D-18-0072.1.

Ávila, E. E., N. E. Castellano, C. P. R. Saunders, R. E. Bürgesser, and G. G. Aguirre Varela, 2009: Initial stages of the riming process on ice crystals. *Geophysical Research Letters*, **36 (9)**, https://doi.org/https://doi.org/10.1029/2009GL037723, URL https://agupubs.onlinelibrary.wiley.com/doi/abs/10.1029/2009GL037723, https://agupubs.onlinelibrary.wiley.com/doi/pdf/10.1029/2009GL037723.